The Astronomical Journal, 165:169 (12pp), 2023 April https://doi.org/10.3847/1538-3881/acbf39

Ground-based Optical Transmission Spectroscopy of the Nearby Terrestrial Exoplanet LTT 1445Ab

Hannah Diamond-Lowe[1,2], João M. Mendonça[1], David Charbonneau[2], and Lars A. Buchhave[1]
[1] National Space Institute, Technical University of Denmark, Elektrovej 328, DK-2800 Kgs. Lyngby, Denmark; hdiamondlowe@space.dtu.dk
[2] Center for Astrophysics | Harvard & Smithsonian, 60 Garden Street, Cambridge, MA 02138, USA
Received 2022 October 3; revised 2023 February 20; accepted 2023 February 24; published 2023 March 21

Abstract

Nearby M-dwarf systems currently offer the most favorable opportunities for spectroscopic investigations of terrestrial exoplanet atmospheres. The LTT 1445 system is a hierarchical triple of M dwarfs with two known planets orbiting the primary star, LTT 1445A. We observe four transits of the terrestrial world LTT 1445Ab ($R = 1.3\ R_\oplus$, $M = 2.9\ M_\oplus$) at low resolution with Magellan II/LDSS3C. We use the combined flux of the LTT 1445BC pair as a comparison star, marking the first time that an M dwarf is used to remove telluric variability from time-series observations of another M dwarf. We find Hα in emission from both LTT 1445B and C, as well as a flare in one of the data sets from LTT 1445C. These contaminated data are removed from the analysis. We construct a broadband transit light curve of LTT 1445Ab from 620 to 1020 nm. Binned to 3 minute time bins, we achieve an rms of 49 ppm for the combined broadband light curve. We construct a transmission spectrum with 20 spectrophotometric bins each spanning 20 nm and compare it to models of clear, 1× solar composition atmospheres. We rule out this atmospheric case with a surface pressure of 10 bars to 3.2σ confidence, and with a surface pressure of 1 bar to 3.1σ confidence. Upcoming secondary eclipse observations of LTT 1445Ab with the James Webb Space Telescope will further probe the cases of a high-mean-molecular-weight atmosphere, a hazy or cloudy atmosphere, or no atmosphere at all on this terrestrial world.

Unified Astronomy Thesaurus concepts: Exoplanet astronomy (486); Exoplanet atmospheres (487); Exoplanets (498); Extrasolar rocky planets (511); Transmission spectroscopy (2133); Spectroscopy (1558); Optical astronomy (1776); M dwarf stars (982)

1. Introduction

The now decommissioned Kepler Space Telescope (Borucki et al. 1997) stared at a single patch of sky for four years and taught us that worlds smaller than about 1.7 $R_\oplus$ are common in the galaxy (Dressing & Charbonneau 2013, 2015; Fressin et al. 2013). However, the vast majority of the small worlds detected by Kepler are too faint for follow-up radial velocity measurements to determine a mass. The space-based Transiting Exoplanet Survey Satellite (TESS; Ricker et al. 2015), along with ground-based surveys like MEarth (Nutzman & Charbonneau 2008; Irwin et al. 2015) and TRAPPIST (Gillon et al. 2013), search the sky for small planets transiting the nearest and brightest stars. Four years into the TESS Mission the number of nearby worlds with $R < 1.7\ R_\oplus$ has grown into the tens, with many having mass measurements or upper limits. Based on both theoretical and empirical evidence (Lopez & Fortney 2013; Owen & Wu 2013; Dressing et al. 2015; Rogers 2015; Fulton et al. 2017; Van Eylen et al. 2018; Luque & Pallé 2022), we can definitively say that there exists a class of exoplanets with measured radii *and* masses consistent with an Earth-like bulk composition. The question then becomes whether or not terrestrial exoplanets can possess substantial atmospheres and if so, what those atmospheres are comprised of.

Unambiguous evidence of an atmosphere around a terrestrial exoplanet has yet to be found. As such, determining whether not a terrestrial exoplanet has an atmosphere at all is a field of active development. Atmospheric circulation models predict that a thick atmosphere ($\gtrsim$1 bar of surface pressure) on a highly-irradiated, tidally-locked world will be able to advect energy from the substellar point toward cooler longitudes (Seager & Deming 2009; Showman et al. 2013; Wordsworth 2015; Koll et al. 2019). The experiment is then to observe a phase curve or secondary eclipse of the terrestrial exoplanet and determine if the planet's dayside thermal emission is reduced compared to the bare-rock case.

Thick high-surface-pressure atmospheres efficiently redistribute heat from the dayside to the nightside; more tenuous, thin atmospheres do not. As such, low-mean-molecular-weight hydrogen- and helium-dominated atmospheres with surface pressures below 10 bar are difficult to detect by their heat-redistribution properties, but are accessible with transmission spectroscopy. Phase-curve observations of the highly-irradiated terrestrial world LHS 3844b resulted in a secondary eclipse depth consistent with a bare rock down to 10 bars of surface pressure (Kreidberg et al. 2019). Follow-up observations in transmission further ruled out low-mean-molecular-weight atmospheres down to 0.1 bars (Diamond-Lowe et al. 2020b), providing further evidence that LHS 3844b is likely a bare rock.

We know from measuring the radii and masses of terrestrial exoplanets that extended hydrogen- and helium-dominated atmospheres making up >1% the planet's mass are highly unlikely (Owen et al. 2020), nor do terrestrial exoplanets possess a significant amount of water by mass that would shift their compositions away from what is measured for the solar system terrestrial worlds (Luque & Pallé 2022). However, it is possible that small amounts (<1% of the planet's mass) of

Table 1
Observations with Magellan II (Clay) and the LDSS3C Multiobject Spectrograph

Data Set Number	Transit Number[a]	Night (UTC)	Time (UTC)	Exp. Time (s)	Duty Cycle (%)	Number of Exposures	Airmass at t_0	Seeing[b] (arcsec)
[c]	56	2019-08-17	…	…	…	…	…	…
[c]	67	2019-10-15	…	…	…	…	…	…
1	75	2019-11-27	01:08:29–05:04:36	15	34.5	326	1.192	0.70–1.10
2	78	2019-12-13	02:34:15–06:46:19	15	34.5	350	1.025	0.60–0.80
[d]	131	2020-09-22	…	…	…	…	…	…
[d]	134	2020-10-08	…	…	…	…	…	…
3	142	2020-11-20	01:40:32–06:05:24	20, 15	41.1, 34.5	215, 127	1.176	1.00–0.45
4	145	2020-12-06	03:28:42–07:39:04	15	34.5	343	1.042	0.50–0.60

Notes.
[a] Transit number is counted from the transit ephemeris $T_0 = 2458412.70851$ (Winters et al. 2022).
[b] Seeing recorded at the beginning and end of observations. Conditions varied during observations 1, 2, and 3.
[c] No data due to bad weather.
[d] No data due to telescope closure in response to the Covid-19 pandemic.

low-mean-molecular-weight material can be retained from the protoplanetary nebula or out-gassed later on, and depending on the history of the terrestrial exoplanet, such an atmosphere may persist. Even a small amount of hydrogen and helium by mass is enough to increase a terrestrial exoplanet's scale height such that its atmosphere is detectable.

For terrestrial worlds orbiting nearby (<15 pc) small ($<0.3)M_\odot$) stars, low-mean-molecular-weight atmospheres are accessible with low-resolution transmission spectroscopy when the planet passes in front of its host star from our line of sight. Employing this technique from both ground- and space-based observatories has delivered a growing number of results that find low-mean-molecular-weight atmospheres on highly-irradiated terrestrial worlds unlikely (de Wit et al. 2016, 2018; Diamond-Lowe et al. 2018, 2020b), while still allowing for heavier, high-mean-molecular-weight atmospheres or no atmospheres at all.

In this work we focus on the terrestrial world LTT 1445Ab (Winters et al. 2019). LTT 1445Ab ($M_p = 2.87^{+0.26}_{-0.25}\ M_\oplus$; $R_p = 1.305^{+0.066}_{-0.061}\ R_\oplus$) orbits the primary star of a hierarchical triple M-dwarf system with a period of $5.3587657^{+0.0000043}_{-0.0000042}$ days (Winters et al. 2022). The measured mass and radius place this world squarely on an Earth-like composition curve. At the time of writing, the LTT 1445A system holds the distinction as being the closest M dwarf to host transiting planets, and given the remaining search space for such worlds, LTT 1445Ab is likely to remain one of the most spectroscopically accessible terrestrial worlds for transmission spectroscopy that we ever find. In this work we present results from four transit observations captured with the Magellan II (Clay) telescope at the Las Campanas Observatory and the LDSS3C multiobject spectrograph. Our optical spectra range from 620 to 1020 nm and we take advantage of the rare case of being able to use the LTT 1445BC M-dwarf binary as a comparison star with which to remove telluric variability during observations.

In Section 2 we explain our observing strategy. Section 3 is dedicated to extracting and analyzing the spectroscopic data. In Section 4 we present the main results of this work and discuss the implications for LTT 1445Ab's atmosphere. We also peer more closely at the LTT 1445BC binary companion and find a broadband flare in one data set and persistent variability in the Hα line across all data sets. We wrap up with our conclusions in Section 5.

2. Observations

The terrestrial exoplanet LTT 1445Ab orbits about its host mid-M-dwarf star every 5.36 days for a duration of 1.38 hr (Winters et al. 2019, 2022), which offers about five opportunities per year to observe a transit event from the Las Campanas Observatory in Chile. We were awarded time for four transit observations on the Magellan II (Clay) telescope in the 2019B semester (PI H. Diamond-Lowe). Two of these were lost due to bad weather. We were awarded a further four transits in the 2020B semester (PI D. Charbonneau), two of which were lost due to observatory closures related to the Covid-19 pandemic. From the 2019B and 2020B semesters we observed a total of four transits of LTT 1445Ab (Table 1). We took spectra before, during, and after the planet transit for a total of 4.75 hr of observing time per transit. Because we did not use a full night and were able to share the telescope with other programs, the observation time included a buffer of 15 minutes (7.5 minutes at the beginning and end of each observation) to change instruments at the telescope.

To capture spectra of LTT 1445A during the planet transit we used the multiobject Low Dispersion Survey Spectrograph (LDSS3C[3]). We used an instrument setup similar to previous programs that involved observing terrestrial exoplanets around nearby M dwarfs (Diamond-Lowe et al. 2018, 2020a, 2020b); however with key differences due to the brightness of LTT 1445A ($V = 11.2$, $T = 8.88$; Henry et al. 2006; Winters et al. 2019) and to the fact that LTT 1445A is part of a hierarchical triple system with two other mid-M dwarfs, LTT 1445B and C.

A multiobject spectrograph where the slit sizes are adjustable is required for low-resolution ground-based time-series observations like these because comparison stars must be observed simultaneously with a target star in order to remove telluric variations imprinted on the stellar spectra during the observations. Comparison stars should be of comparable magnitude to the target star in the bandpass of observations, which means that usually M dwarfs are compared to spectrally different FGK stars. In this case, the combined spectra of the companion M dwarfs LTT 1445BC can be used as a comparison star to LTT 1445A, marking the first time that an M dwarf can be compared to another M dwarf in multiobject spectroscopy for the purposes of constraining a planetary atmosphere. We note that

[3] LDSS3C Technical Specifications (http://www.lco.cl/?epkb_post_type_1=ldss3_c-2).

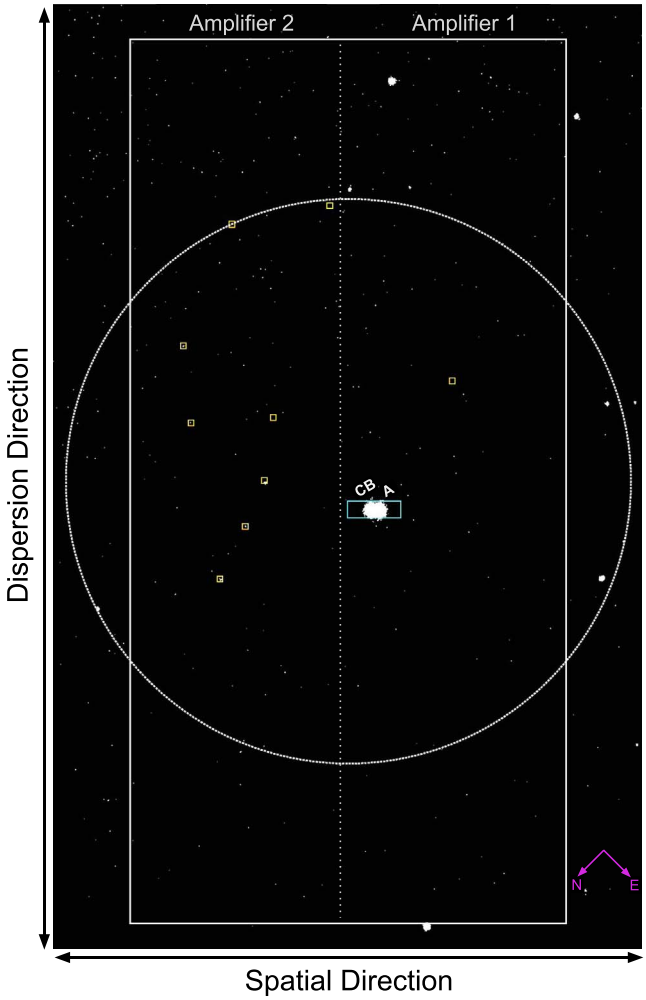

Figure 1. Image of the LTT 1445 field in 2019 September from MEarth South (Nutzman & Charbonneau 2008; Irwin et al. 2015), which is available through the ExoFOP-TESS portal[4]. The large circle shows the field of view of LDSS3C, and the solid rectangle is the extent of the LDSS3C detector. The two LDSS3C amplifiers are labeled at the top of the detector rectangle, with the vertical dotted line indicating the split on the detector. The light blue rectangle is the 47″ × 15″ slit for LTT 1445ABC. Orange squares indicate small slits for alignment stars.

given the alignment of the LTT 1445 stars we are effectively using a single slit as opposed to multiple slits (Figure 1).

We place all three stars in the LTT 1445 system in the same slit on the science mask, 47″ wide in the cross-dispersion direction and 15″ in the dispersion direction (Figure 1). This allows us to measure 20″ of sky background on either side of LTT 1445A and the LTT1445BC pair, as well as enough room in the dispersion direction to guard against light losses. The calibration mask is identical to the science mask but with 0.″5 slits in the dispersion direction. During the afternoon prior to observations we take biases, darks, and quartz flats with the science mask, as well as helium, neon, and argon arcs with the calibration mask. During night-time observations we take a set of undispersed reference images with the science mask before and after the main science images in order to mark the location of the LTT 1445 stars on the detector. These undispersed images with the science mask are useful during data extraction.

[4] https://exofop.ipac.caltech.edu/tess/index.php

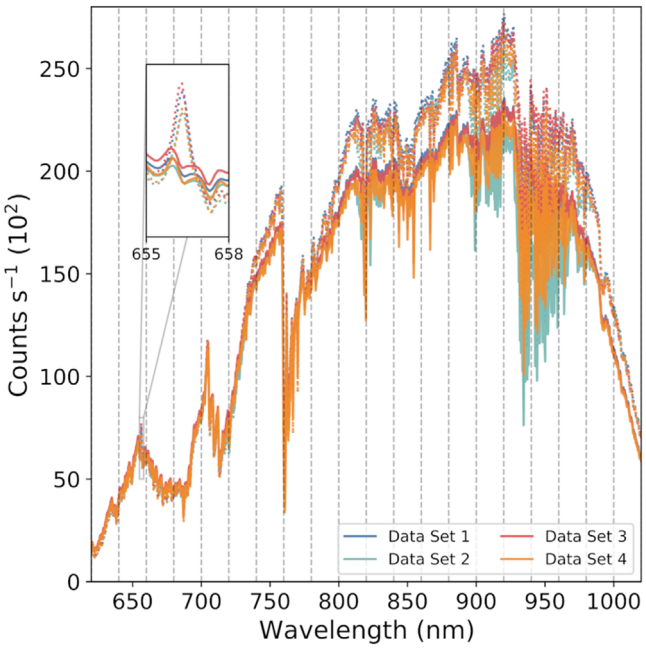

Figure 2. Average spectra of LTT 1445A (solid lines) and LTT 1445BC combined (dotted lines) from each of the 4 data sets. The spectra represent the total counts from each star measured over the course of each observing night, normalized by the total integration time (exposure time × number of exposures). Vertical gray lines are the edges of the 20 nm spectrophotometric bands. The inset zooms in on the Hα line, which is evident in emission in the combined LTT 1445BC comparison star, but not in LTT 1445A.

Table 2
GP Regression Data

Input Regressors	Data Set Number			
	1	2	3	4
Airmass		✓		✓
Rotation angle	✓	✓		✓
Centroid	✓	✓	✓	✓
Width	✓	✓	✓	✓
Peak			✓	
Shift			✓	✓
Stretch				
Time			✓	

Note. A more detailed explanation of these regressors can be found in Diamond-Lowe et al. (2020a).

With LDSS3C we use the `1x1` detector binning, `Turbo` readout speed, and `Low` gain settings. These settings accommodate the brightness of the LTT 1445 stars. According to the LDSS3C User Manual,[5] the `Turbo` readout speed is not supported for science observations due to variable readout noise that can adversely affect data taken for faint sources. For this mode the read noise is 8 e^- rms (Stevenson et al. 2016). In the case of the LTT 1445 stars we are far from the read noise limit, so we use the `Turbo` readout mode to improve the observing cadence (Stevenson et al. 2016; A. Seifahrt 2023, private communication). For most of the observations we took 15 s exposures with 28.5 s readout time, bringing the duty cycle to 34.5%. At the start of observations for Data Set 3 seeing conditions were poor so we increased the exposure time to 20 s, however during

[5] LDSS3C User Manual (http://www.lco.cl/?epkb_post_type_1=ldss-3-user-manual).

Table 3
Broadband Light-curve Transit Parameters and Priors

Parameter	Prior	Data Set Number			
		1	2	3	4
$\delta\ t_0$ (days)[i]	$\mathcal{U}$ (−0.001, 0.001)[ii]	-0.00019 ± 0.00009	-0.00025 ± 0.00011	0.00015 ± 0.00007	0.00021 ± 0.00016
R_p/R_s	$\mathcal{U}$(0.02, 0.07) [ii]	0.0432 ± 0.0010	0.0447 ± 0.0009	0.0443 ± 0.0008	0.0439 ± 0.0008
cos i	$\mathcal{U}$(0.0, 1.0) [ii]	$0.0052^{+0.0045}_{-0.0031}$	$0.0094^{+0.0056}_{-0.0047}$	$0.0059^{+0.0046}_{-0.0036}$	$0.0118^{+0.0079}_{-0.0068}$
a/R_s	$\mathcal{U}$(5, 100) [ii]	$31.33^{+0.37}_{-0.95}$	$30.39^{+0.99}_{-1.76}$	$31.00^{+0.45}_{-1.05}$	$29.62^{+1.59}_{-2.81}$
l_0	$\mathcal{N}$(0.43, 0.19) [ii]	0.42 ± 0.17	0.44 ± 0.15	0.53 ± 0.15	0.46 ± 0.16
l_1	$\mathcal{N}$(0.58, 0.06) [ii]	0.568 ± 0.052	0.573 ± 0.044	0.619 ± 0.042	0.572 ± 0.047
	Rms (ppm)[iii]	124	207	115	289

Notes.
[i] $\delta\ t_0$ is the difference between the predicted time of midtransit and the derived time of midtransit from fitting each broadband light curve. The predicted time of midtransit is calculated as $t_0 = T_0 + nP$ where $T_0 = 2458412.70851$ BJD_{TDB} and $P = 5.3587657$ days (Winters et al. 2022); n is the transit number given in Table 1 for each transit. All resulting $\delta\ t_0$ values are less than the observation cadence time of approximately 48 s per integration (15 or 20 s exposure time plus readout time).
[ii] $\mathcal{U}$ stands for uniform prior; $\mathcal{N}$ stands for Gaussian prior.
[iii] The rms values are calculated by comparing the unbinned broadband light-curve residuals to the GP model for each data set.

observations seeing improved dramatically and we reduced the exposure time to 15 s shortly after transit egress in order to avoid saturating any detector pixels (Table 1).

LDSS3C's 16-bit analog-to-digital converter has a saturation limit of 65,535 analog-to-digital units (ADUs). We ensure that all pixels used in the data analysis stay under this limit during observations. Given that the gains listed in the LDSS3C User Manual are out of date, the LDSS3C instrument specialists at Las Campanas Observatory made updated gain measurements in each of the two CCD amplifiers during the observing season. For the 2019 observations we use gains of 2.95 e^- ADU^{-1} and 2.56 e^- ADU^{-1} for amplifiers 1 and 2, respectively, to convert the measured ADUs to photoelectrons. For the 2020 observations we use gains of 2.84 e^- ADU^{-1} and 2.52 e^- ADU^{-1}, respectively.

3. Data Extraction and Analysis

Our data extraction and analysis steps are nearly identical to those outlined in Diamond-Lowe et al. (2020a, 2020b). We use the `mosasaurus` [6] extraction pipeline to turn the raw images taken at the telescope into data cubes that include time series of wavelength calibrated 1D spectra for each star in each data set (we treat LTT 1445BC as a single star in the extraction; Figure 2). We also record auxiliary information collected during the observations and subsequent extraction; for example, the airmass and instrument rotation angle at the time of each integration and the average widths of the stellar spectral traces on the detector over the course of the time series, which is a proxy for seeing conditions during observations.

Using the LTT 1445BC pair as the comparison star yields two main differences as compared to previous extraction and analysis steps described in Diamond-Lowe et al. (2020a, 2020b). The first occurs during wavelength calibration. After an initial wavelength solution is found using calibration arcs, we then perform a finer calibration where we cross-correlate elements of each spectrum with a master spectrum. This resulting wavelength correction is determined for every spectrum and for every data set. Usually the cross-correlation step would use telluric features (e.g., oxygen and water lines) as well as prominent stellar features (e.g., Ca II triplet lines) to finely align the spectra. In this case, LTT 1445BC is the same spectral type as the target star LTT 1445A so we can cross-correlate against the entire spectrum, not just a subset of features. We divide the spectra up into 10 chunks in order to allow for both a shift and stretch in the spectra during the course of observations. Using the LTT 1445BC M-dwarf pair as a comparison star provides a marked advantage during wavelength calibration, especially at the edges of the spectra where low counts can make cross-correlating with telluric features difficult.

The second difference in this data set is that the LTT 1445BC time series exhibits variability around the Hα line, which is not the case for LTT 1445A (Figure 2). Because this variability is not telluric but rather inherent to one or both of the LTT 1445BC components, we cannot use any spectral information around the Hα line when using LTT 1445BC to remove broad telluric variability from the LTT 1445A time series. We therefore exclude data between 655 and 658 nm when performing the analyses. In Data Set 1 we also capture a broadband flare in the LTT 1445BC component. We exclude the four time points associated with this flare from the broadband and spectrophotometric analysis of Data Set 1. The flare and Hα variability in the BC component is further discussed in Section 4.2.

We construct broadband light curves by summing all of the flux (with the exception of the Hα line) from 620 to 1020 nm. We fit the light curve using a Gaussian process (GP) regression with a Matérn 3/2 kernel (`george`; Ambikasaran et al. 2015) that takes a transit model (`batman`; Kreidberg 2015) as the mean function. For each data set we fit for the time of midtransit t_0, planet-to-star radius ratio R_p/R_s, the cosine of the inclination cos i, the scaled semimajor axis a/R_s, and two logarithmic limb-darkening parameters l_0 and l_1, which are reparameterized according to Espinoza & Jordán (2016). We place Gaussian priors on the reparameterized limb-darkening coefficients set by the mean and five times the uncertainty given by the Limb Darkening Toolkit (`LDTk`; Parviainen & Aigrain 2015). We assume a circular orbit ($e = 0$) since stand-alone transits like the ones we present here provide negligible information on a planet's eccentricity.

[6] https://github.com/zkbt/mosasaurus

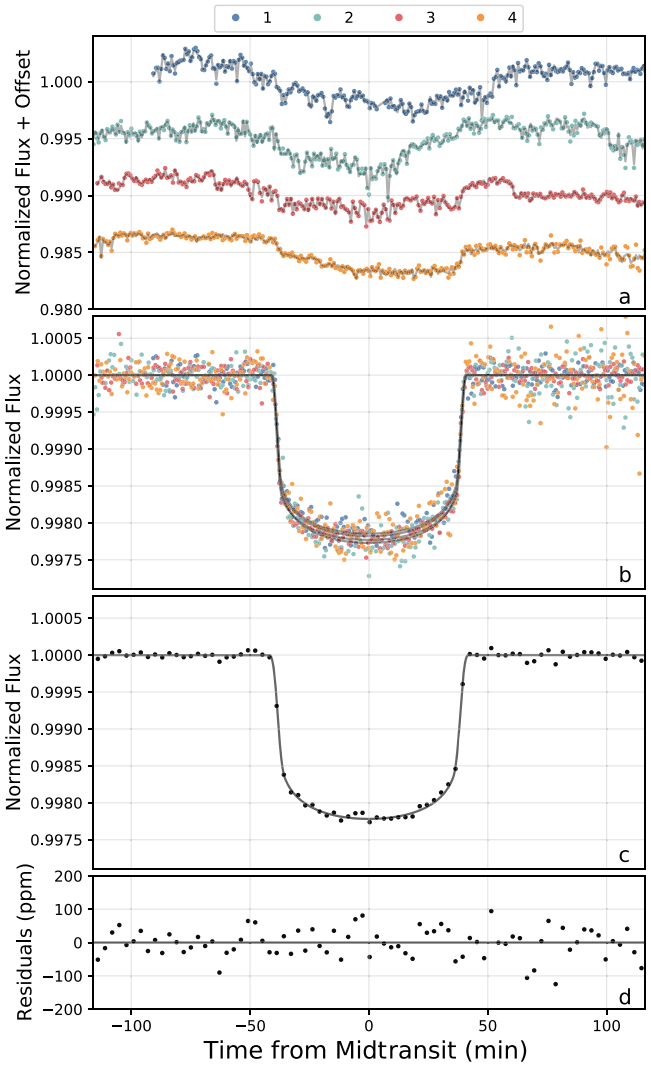

Figure 3. Panel (a): broadband light curves of four transit observations of LTT 1445Ab. Each color represents a different data set, corresponding to the data set numbers in Table 1. The combined transit and GP noise model is shown in gray. The raw light curves are highly correlated with the width and centroid vectors from the LTT 1445BC spectral trace. These regressors, preferred in every data set, are responsible for the strong variation in the GP noise models. Panel (b): same as panel (a) but with the GP noise component removed. The rms of the combined light curve is 200 ppm. Panel (c): same as panel (b) but with the combined light curve binned to 3 minutes time bins. The transit model is smoothed using a 3 minutes box-car kernel. The rms of the 3 minutes binned combined light curve is 49 ppm. Panel (d): residuals of panel (c).

We use a dynamic multinested sampler (`dynesty`; Speagle 2020) to explore the parameter space. Following Diamond-Lowe et al. (2020b), we test several vectors containing auxiliary information, such as airmass, centroid, etc., to use as regressors in the GP, and select the best combination according to the Bayesian evidence output from `dynesty`. The regressors used for each data set can be found in Table 2. The best-fit values and figures from the broadband light-curve analysis can be found in Table 3 and Figure 3. Our best-fit orbital parameters from the broadband fit are in excellent agreement with those of Winters et al. (2022). Since the initial preparation of this manuscript, Lavie et al. (2022) provided an update to the orbital parameters of LTT 1445Ab using both TESS transit data and VLT/ESPRESSO radial velocity data. There is some discrepancy between their reported orbital parameters for LTT 1445Ab and those of Winters et al. (2022) and this work. Further analysis beyond the scope of this work is necessary to resolve these discrepancies.

The spectra of LTT 1445BC are not completely resolved on the detector so we use the combined spectrum of this binary pair as a comparison star to LTT 1445A. We note that the resulting light curves are highly correlated with the changing width and centroid of the LTT 1445BC spectral trace, likely because `mosasaurus` is built to fit one Gaussian profile instead of two.[7] When fitting the light curves with a Gaussian process the width and centroid vectors are unsurprisingly favored as regressors in every data set. We also do not necessarily need to include airmass as GP regressor since there is negligible differential extinction between the comparison and target stars (though Data Sets 2 and 4 still prefer the use of airmass as a regressor).

For each data set we divide the broadband spectra into 20 nm spectrophotometric bands and sum up the flux in each band to create 20 spectral light curves. We perform a GP regression on each of these spectral light curves, allowing the hyperparameters to vary but using the same set of regressors as for the broadband light curves. For the spectral light curves we fix t_0, $\cos i$, and a/R_s to the best value from the broadband light-curve fit and then fit for R_p/R_s, l_0, and l_1 for each data set. We provide the resulting spectrophotometric transit depths for each data set, as well as the inverse-variance weighted average transit depths, in Table 4 and Figure 4.

4. Results and Discussion

4.1. Transmission Spectrum of LTT 1445Ab Compared to Atmospheric Models

To create our transmission spectrum, we take the inverse-variance weighted mean of the transit depths in each spectrophotometric band (Figure 5). We can then compare this observed transmission spectrum to model transmission spectra of LTT 1445Ab to test the likelihood of a set of 1× solar composition ($\mu = 2.3$ g mol^{-1}) atmospheric cases with surface pressures ranging from 0.01 to 10.0 bars.

To build the model transmission spectra we first determine temperature–pressure (T–P) profiles for each atmospheric case using a 1D radiative-convective model developed in Mendonća & Buchhave (2020). The code uses a two-stream formulation with multiple scattering effects to represent the radiative processes in the atmosphere (Mendonća et al. 2015). To ensure that the vertical gradient of the temperature does not exceed the adiabatic profile, we use a simple convective adjustment scheme to mix the enthalpy instantaneously in a buoyant unstable atmospheric region (Mendonća et al. 2018; Malik et al. 2019b). Our radiative transfer code uses an opacity (κ) table with a correlated-κ approximation as described in Malik et al. (2017) and the same parameters as in Malik et al. (2019a). The cross-sections in the κ-distribution table are computed using the `HELIOS-K` software (Grimm et al. 2021) from the following line lists: H_2O (Barber et al. 2006), CO_2 (Rothman et al. 2010), CO (Li et al. 2015), CH_4 (Yurchenko & Tennyson 2014), NH_3 (Yurchenko et al. 2011), HCN (Harris et al. 2006), C_2H_2 (Gordon et al. 2017), PH_3 (Sousa-Silva et al. 2015), H_2S (Azzam et al. 2016), Na and K (Burrows et al.

[7] In attempting to separate the B and C components we fitted a double Gaussian profile to the LTT 1445BC trace, but were unable to achieve satisfactory results.

Table 4
Spectroscopic Transit Depths

Wavelength (nm)	Transit Depths $(R_p/R_s)^2$ by Data Set (%)				Mean $(R_p/R_s)^2$ (%)	rms (ppm)	× Exp. Noise
	1	2	3	4			
620–640	0.1434 ± 0.0393	0.1734 ± 0.0192	0.2340 ± 0.0443	0.1875 ± 0.0117	0.1836 ± 0.0095	680	1.32
640–660[a]	0.1623 ± 0.0198	0.1920 ± 0.0125	0.2003 ± 0.0233	0.1883 ± 0.0094	0.1874 ± 0.0067	502	1.31
660–680	0.1826 ± 0.0263	0.2041 ± 0.0139	0.1951 ± 0.0339	0.1994 ± 0.0099	0.1992 ± 0.0075	508	1.37
680–700	0.1599 ± 0.0227	0.1874 ± 0.0109	0.2071 ± 0.0251	0.2000 ± 0.0090	0.1929 ± 0.0064	471	1.35
700–720	0.1860 ± 0.0184	0.1949 ± 0.0098	0.1829 ± 0.0207	0.2001 ± 0.0085	0.1955 ± 0.0058	402	1.38
720–740	0.1465 ± 0.0180	0.2028 ± 0.0077	0.1922 ± 0.0131	0.1904 ± 0.0073	0.1923 ± 0.0047	365	1.53
740–760	0.1949 ± 0.0112	0.1966 ± 0.0074	0.1894 ± 0.0065	0.2002 ± 0.0069	0.1950 ± 0.0037	313	1.55
760–780	0.1608 ± 0.0161	0.2016 ± 0.0082	0.2130 ± 0.0136	0.1930 ± 0.0079	0.1958 ± 0.0050	355	1.51
780–800	0.1893 ± 0.0117	0.1974 ± 0.0074	0.1999 ± 0.0088	0.1993 ± 0.0073	0.1976 ± 0.0042	308	1.52
800–820	0.1850 ± 0.0091	0.1966 ± 0.0064	0.2026 ± 0.0064	0.2050 ± 0.0066	0.1989 ± 0.0034	290	1.55
820–840	0.1703 ± 0.0106	0.2024 ± 0.0065	0.1964 ± 0.0071	0.1936 ± 0.0065	0.1943 ± 0.0036	297	1.63
840–860	0.1892 ± 0.0100	0.1963 ± 0.0058	0.1937 ± 0.0128	0.1983 ± 0.0075	0.1955 ± 0.0040	283	1.55
860–880	0.2009 ± 0.0088	0.2038 ± 0.0064	0.1904 ± 0.0074	0.1998 ± 0.0068	0.1990 ± 0.0036	282	1.60
880–900	0.2090 ± 0.0079	0.1941 ± 0.0059	0.1933 ± 0.0059	0.1880 ± 0.0061	0.1946 ± 0.0031	270	1.55
900–920	0.2019 ± 0.0095	0.2013 ± 0.0059	0.1942 ± 0.0066	0.1906 ± 0.0061	0.1964 ± 0.0033	280	1.63
920–940	0.1979 ± 0.0104	0.1950 ± 0.0065	0.1897 ± 0.0057	0.2056 ± 0.0063	0.1965 ± 0.0033	285	1.55
940–960	0.2216 ± 0.0051	0.1967 ± 0.0059	0.1851 ± 0.0053	0.1912 ± 0.0062	0.1998 ± 0.0028	275	1.42
960–980	0.2200 ± 0.0122	0.1904 ± 0.0098	0.1881 ± 0.0077	0.2018 ± 0.0079	0.1972 ± 0.0044	315	1.61
980–1000	0.2045 ± 0.0166	0.1850 ± 0.0082	0.1830 ± 0.0083	0.1903 ± 0.0075	0.1877 ± 0.0044	366	1.73
1000–1020	0.2221 ± 0.0072	0.1911 ± 0.0103	0.1803 ± 0.0107	0.1950 ± 0.0090	0.2022 ± 0.0045	486	1.80

Notes. The final three columns provide the inverse-variance weighted mean across all four data sets for each spectroscopic band, along with the rms of the four data sets combined in each band. The final column, × Expected Noise, describes how close, on average, we get to the calculated photon noise in each band.
[a] This spectral band excludes wavelengths covering the Hα line (655–658 nm).

2000; Burrows & Volobuyev 2003; Kurucz 2011), collision-induced absorption of H_2–H_2 (Richard et al. 2012) and H_2–He (Richard et al. 2012), and scattering cross-sections of H_2 (Sneep & Ubachs 2005) and H (Lee & Kim 2004).

We calculate the chemical concentrations with the open-source code `FastChem` (Stock et al. 2018), with a constant surface albedo set to 0.2. All simulations are integrated until radiative-convective equilibrium is reached (Malik et al. 2017). We then feed these custom *T*–*P* profiles into the publicly available `Exo_Transmit` code (Miller-Ricci Kempton et al. 2012; Kempton et al. 2017) in order to generate model transmission spectra. Similar to the use of model transmission spectra in Diamond-Lowe et al. (2018, 2020a, 2020b), we allow the surface radius of LTT 1445Ab to vary in the model until we get a result that most closely matches the observed transmission spectrum based on the reduced χ^2 statistic, thereby accounting for our uncertainty in the true radius at the solid planet surface.

We compare the model transmission spectra to the observed transmission spectrum (Figure 6). We disfavor a clear, solar composition atmospheres at 10 bars of surface pressure at 3.2σ confidence, and 1 bar to 3.1σ. The observed transmission spectrum is consistent with tenuous solar composition atmospheres with 0.1 bar and 0.01 bar of surface pressure or higher-mean-molecular-weight atmospheres dominated by heavier species such as H_2O, CO_2, or O_2. It is also possible that LTT 1445Ab is devoid of an atmosphere.

The presence of an aerosol layer on LTT 1445Ab would also hinder our ability to detect its atmosphere. At low resolution an aerosol layer would act as the de facto bottom of the atmosphere, truncating any spectral features below it. This means that with our observed transmission spectrum we can rule out a high pressure (low altitude) aerosol layer at 1 bar or higher, but a low pressure (high-altitude) aerosol layer is degenerate with the cases of a tenuous (0.1 bar or less) atmosphere or no atmosphere. Probing the cases of an aerosol-rich atmosphere on LTT 1445Ab would require broader wavelength coverage or higher resolution spectral information.

We note that the transmission spectrum derived from Data Set 1 (blue bars in Figure 5) is discrepant from the others in several spectroscopic bands and appears to have a downward slope toward bluer wavelengths. Such slopes have been interpreted as evidence of unocculted bright spots, or faculae, on the surface of the star (e.g., Rackham et al. 2017 for the sub-Neptune GJ 1214b). These effects are multiplicative with transit depth, and so unlikely to be observable in LTT 1445Ab's transmission spectrum at the precision we are able to achieve with Magellan/LDSS3C. We find a more plausible explanation in an overall increase in variability in the LTT 1445BC comparison star in Data Set 1 (see Section 4.2). As a test we remove Data Set 1 from the analysis, and find that we are able to rule out the 10 and 1 bar atmospheric cases to even higher confidence (4.8σ and 4.7σ, respectively).

4.2. Flaring and Hα Variability in LTT 1445BC

Analysis of two sectors of TESS data reveals that one or both of the BC components in the LTT 1445 system exhibits flare activity and Hα in emission (Winters et al. 2019, 2022). Using X-ray time series observations by the Chandra X-ray Observatory, Brown et al. (2022) are able to resolve the A, B, and C, components of the LTT 1445 system and determine that C is the brightest X-ray source of the three stars, making it a likely candidate for the origin of the activity signal. We identify a flare in Data Set 1 originating from LTT 1445BC, as well as time-varying Hα emission LTT 1445BC in all four data sets. We first investigate the Hα emission from LTT 1445BC

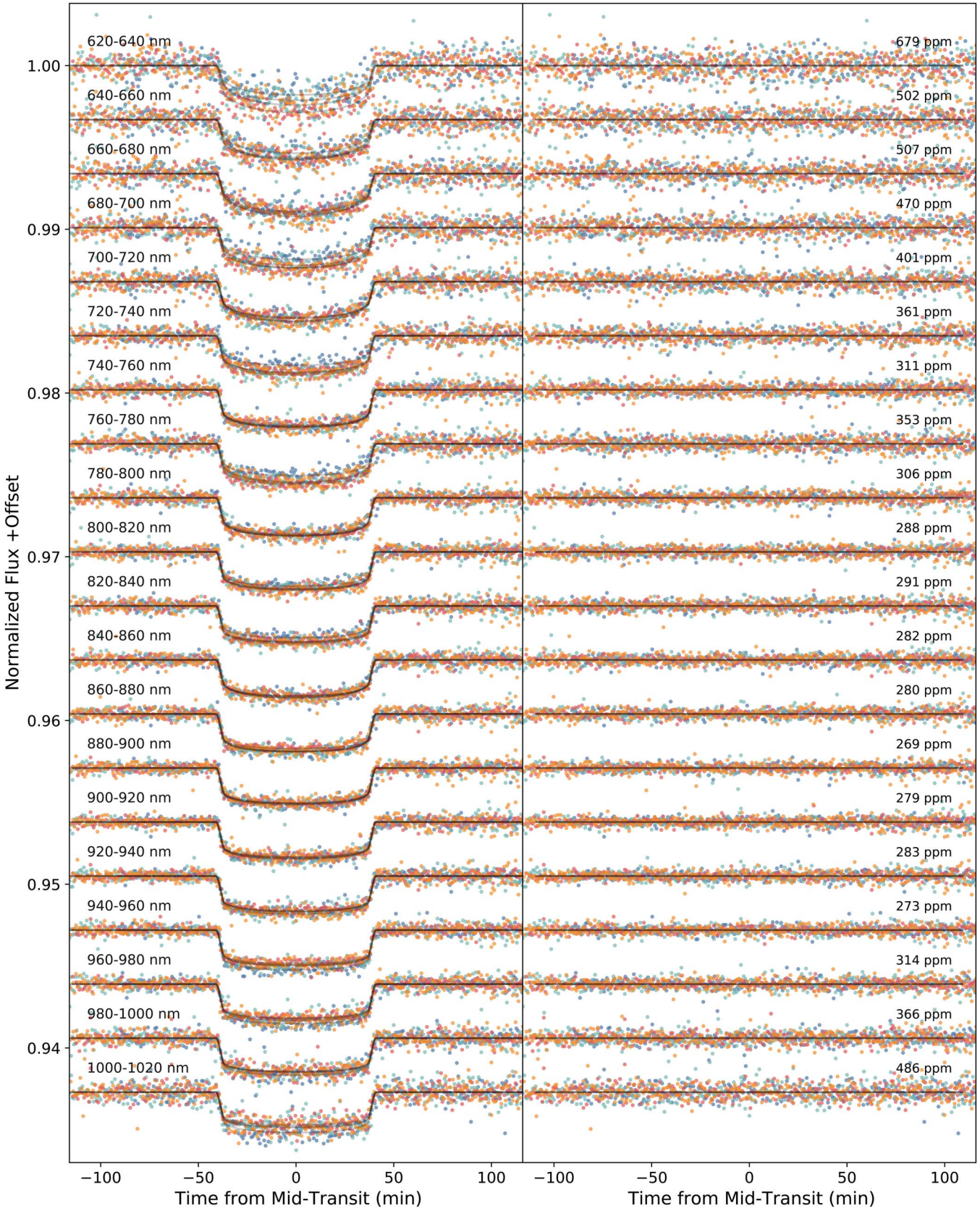

Figure 4. Left: spectroscopic light curves with the GP noise component removed for each of the 4 data sets. The transit model (GP mean function) is plotted in gray for each data set. Light curves are offset for clarity. Right: residuals compared to the best-fit transit model for each of the four data sets along with the combined rms. The individual transit depths and uncertainties are provided in Table 4 and shown in Figure 5.

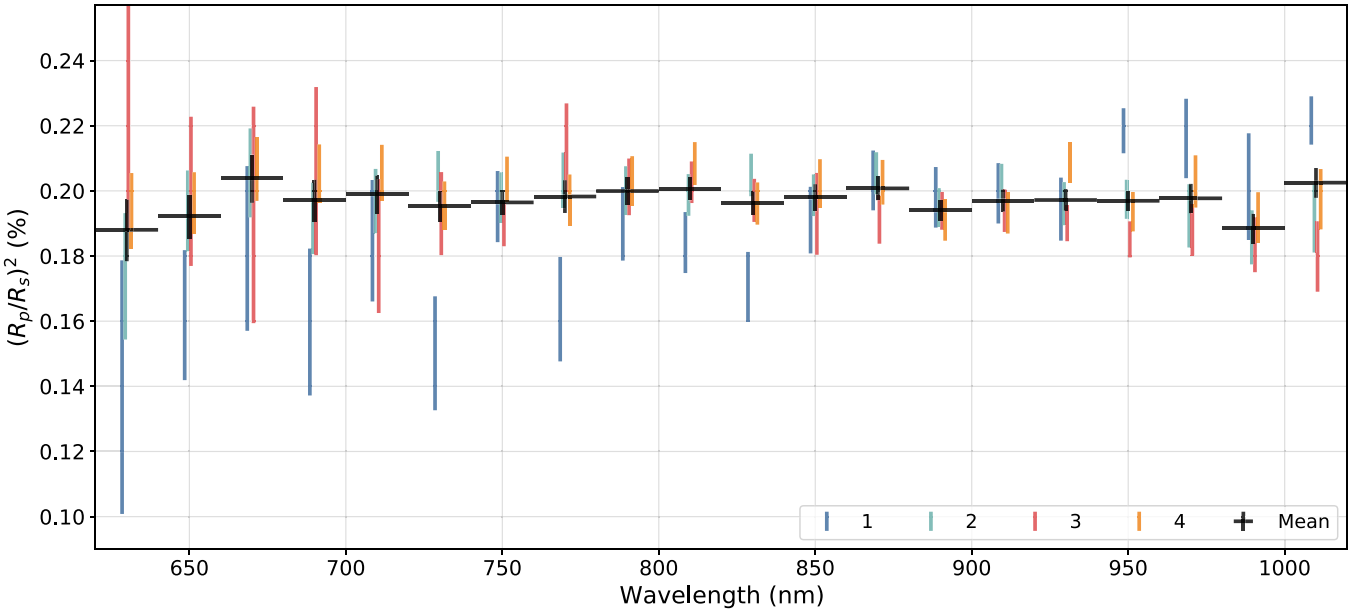

Figure 5. Transmission spectra from Data Sets 1–4. The spectroscopic data are binned to 20 nm and the individual transmission spectra are offset for clarity in the x-axis. Bars in the y-axis represent 68% confidence intervals, with black bars representing the inverse-variance weighted mean value of $(R_p/R_s)^2$ in each bin; black bars along the x-axis illustrate the extent of each bin in wavelength.

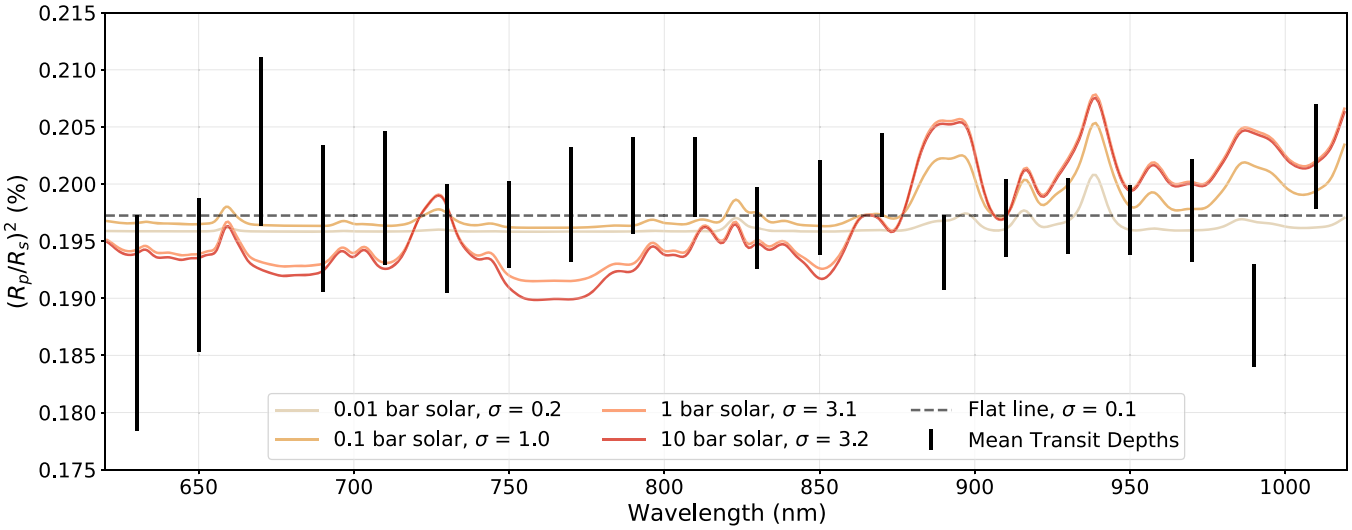

Figure 6. Observed transmission spectrum of LTT 1445Ab from four data sets combined (black points the same as in Figure 5) compared to model transmission spectra derived from 1× solar composition atmospheres from 0.01 to 10 bars of surface pressure. The σ values in the legend are the confidence to which we can rule out the corresponding model transmission spectrum. We confidently rule out (to 3.2σ) a 1× solar composition atmosphere with 10 bars of surface pressure, and (to 3.1σ) the same atmosphere with with 1 bar of surface pressure.

and then try to determine which component the flare and variability arise from.

4.2.1. LTT 1445BC as One Source

We construct (1) broadband light curves for LTT 1445BC that include the Hα wavelengths (left out in the main analysis), and (2) narrow Hα-band light curves to investigate the Hα variability. To construct the LTT 1445BC light curves we use the primary star LTT 1445A to remove telluric and instrumental variation from LTT 1445BC. LTT 1445A is Hα-quiet and does not exhibit any variability during the four observations. When removing systematics from these light curves we find that the GP regression is too flexible and removes some of the astrophysical variability we are trying to focus on, particularly in the Hα-only light curves. We instead opt to use a simple linear decomposition using of all possible regression vectors provided in Table 2 (similar to the analysis method described in Diamond-Lowe et al. 2018). Though this process removes known correlated noise, some correlated noise from an unknown source remains in these light curves. We do not perform any outlier clipping of the light curve so as to preserve flare points.

We remove the LTT 1445Ab transit from the LTT 1445A light curve by fixing the transit parameters to those of the best-fit transit broadband transit (in the case of the broadband light curves) and the best-fit transit in the 640–660 nm spectroscopic

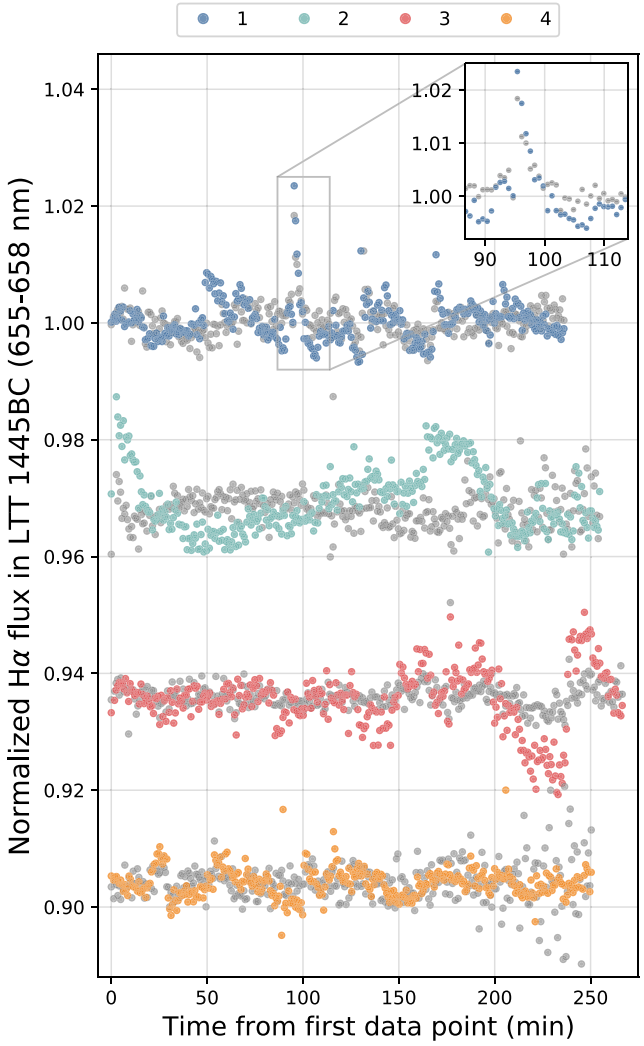

Figure 7. Normalized Hα (655–658 nm) light curves from LTT 1445BC in each of the four data sets analyzed in this work. Gray points in the background are the integrated broadband flux in each data set. The data are not flux calibrated so the light curves are presented as normalized flux. We multiply the broadband flux variability (gray points) by a factor of 10 so as to easily compare to the variability in the Hα-only light curves. The inset shows a broadband flare identified in Data Set 1.

band (for the Hα light curves). We can then remove this exact transit shape from the LTT 1445A light curve. After removing the best-fit transit and systematics model, we simply invert the light curve such that that BC component is divided by the A component, instead of the other way around. This way a flare from the BC component will appear as an increase in flux, instead of a decrease in flux.

In Figure 7 we present the variability in Hα flux (655–658 nm) in Data Sets 1–4. For comparison, we plot the broadband light curves behind in gray. The data are not flux calibrated so we only present normalized Hα and broadband light curves. The broadband data have inherently less scatter since we sum over all wavelengths, so we multiply the existing scatter by a factor of 10 in order to compare it more easily to the Hα variability. It is clear that some variability in the Hα flux is actually due to an overall trend in flux—for example, the first 20 minutes of Data Set 2 show a distinct slope in both the broadband and Hα flux that was not removed by the linear regression. However, between minutes 150 and 200 of the same data set there is clear variability in the Hα flux where the broadband flux remains stable. We also zoom in on the flare in Data Set 1, which occurs at all wavelengths. This is why, as stated in Section 3, we remove the data points associated with the flare in Data Set 1, and the Hα wavelengths from all data sets.

We additionally search the combined BC spectra for emission and variability in other known bands related to activity indicators, such as K I (7664.90, 7698.96 Å), Na I (8183.26, 8194.82 Å), and Ca II (8498.02, 8542.09, 8662.14 Å), which are detected in the more active M dwarf, Proxima Centauri (Robertson et al. 2016). We do not see evidence of these lines, either because LTT 1445BC lacks these indicators, or because our data are taken at relatively low resolution ($R \sim 1000$). In either case, we see no evidence of additional variability from the BC component imprinting on the spectroscopic light curves and resulting transit depths.

4.2.2. Separating LTT 1445B and C in Hα

The spectra of LTT 1445B and C cannot be fully separated in the Magellan II/LDSS3C data, especially in the redder part of the spectrum (>700 nm in Figure 2) where the point-spread function of the two stars in the spatial direction becomes completely blended. However, the Hα line at the blue end of the spectra where M dwarfs emit few photons, can be seen by eye in the raw data (Figure 8). From this raw data we sum up the rows in the spatial direction associated with each star and plot the spectrum. Hα can be seen in emission for both LTT 1445B and C, and is absent from LTT 1445A, as expected.

We then determine which component, B or C, is responsible for the flare in Data Set 1. We take the raw exposures around the time of the flare and sum up the flux in a box of pixels centered on the Hα line for B and C, and can determine that LTT 1445C is the origin of the flare in Data Set 1 (Figure 8). Looking at the whole time series, we additionally find that C is responsible for the bulk of the Hα variability in Data Set 1, and that Data Set 1 exhibits overall more variability than Data Sets 2, 3, and 4.

Time-varying Hα emission is a well-measured phenomenon in M dwarfs (e.g., Lee et al. 2010). High levels of Hα activity are correlated with rapid stellar rotation periods (Newton et al. 2016, 2018; Medina et al. 2020), though Hα variability has not been shown to correlate with rotational phase (Medina et al. 2022). Instead, Medina et al. (2022) posit that low-energy flares are responsible for the observed Hα variation. The variation seen in the Magellan II/LDSS3C Hα light curves occurs on timescales of minutes to hours, and is ultimately undetectable in the broadband light curves (which cover approximately the same spectral range as TESS). It is only when we zoom in to the Hα band that this rich variability revealed, suggesting that short timescale Hα variability is hidden in the broadband photometric TESS data, especially since the more active LTT 1445C is fainter than B at optical wavelengths. That LTT 1445C is the more active component is in agreement with rapid rotation rate estimates (Winters et al. 2019), and with X-ray data showing that LTT 1445C is the brightest X-ray source in the system (Brown et al. 2022).

Based on two sectors of TESS data (Sectors 4 and 31), as well as a year of ground-based photometric monitoring of the LTT 1445 system by MEarth (Nutzman & Charbonneau 2008; Irwin et al. 2015), Winters et al. (2022) estimate a 1.4 days

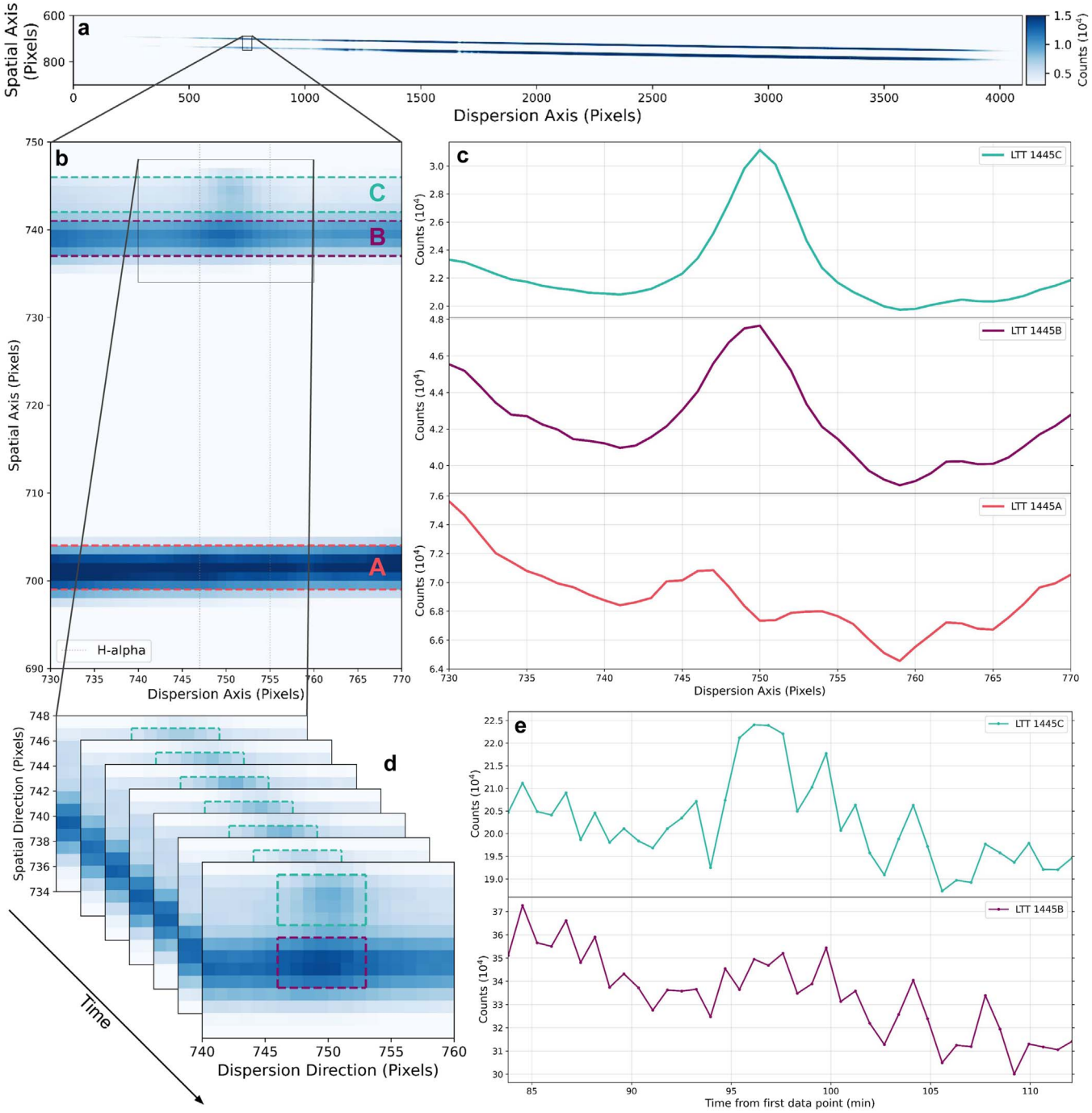

Figure 8. Steps to separate the Hα spectra in time series of LTT 1445B and C from Data Set 1. Panel (a): stacked spectrum of raw images from Data Set 1. Panel (b): zoomed in to the spectral region around the Hα line. Hα emission is visible by eye in stars B and C, but not in A. Panel (c): pixels are summed in the spatial direction, as indicated by the dashed lines in Panel (b), and plotted along the dispersion axis. Hα is present in emission for both LTT 1445 B and C. Panel (d): we sum the counts in a box of pixels around the Hα lines in both B and C as indicated by the dashed lines. We do this for each exposure across the time span where we see the flare in Data Set 1. Panel (e): counts as a function of time for B and C. It is clear that the flare in Data Set 1 occurring around the 95th minute after the start of the time series originates from LTT 1445C.

rotation period for LTT 1445C and perhaps a 6.7 days rotation period for LTT 1445B. While our narrowband Hα observations demonstrate clear variability, these observations span 4.2 hr, or about 12.5% of the dominant 1.4 days rotation period seen in the TESS data. The four Magellan/LDSS3C data sets presented here are taken from one month to one year apart (Table 1), so these data do not represent consistent time coverage comparable to the TESS data. The relatively short time coverage of the Magellan II/LDSS3C data is too sparse to further constrain the larger rotational variation of LTT 1445B or C.

5. Conclusion

We observed four transits of the nearby exoplanet LTT 1445Ab using the ground-based multiobject spectrograph LDSS3C mounted on the Magellan II (Clay) telescope at the Las Campanas Observatory in Chile. A particular advantage of

observing the LTT 1445 system is that the close binary pair LTT 1445BC can be used as a comparison star to LTT 1445A when removing telluric variability during observations. LTT 1445A is well separated from the LTT 1445BC binary pair, but we are unable to fully resolve the spectra of the B and C components in our data. However, we do determine that LTT 1445C is responsible for the bulk of the Hα variation seen in the LTT 1445BC light curves, as well as for a flare detected in Data Set 1. When constructing broadband and spectroscopic light curves for analysis we exclude the flare time points from the Data Set 1 and all spectral data in the Hα band (655–680 nm).

With the data presented in this work we rule out a clear, low-mean-molecular-weight atmosphere at 10 bars of surface pressure (3.2σ) and 1 bar of surface pressure (3.1σ). This result joins previous work on GJ 1132b (Diamond-Lowe et al. 2018; Mugnai et al. 2021; Libby-Roberts et al. 2022), TRAPPIST-1a–f (de Wit et al. 2016, 2018), LHS 3844 (Diamond-Lowe et al. 2020b), L 98-59b–d (Damiano et al. 2022; Zhou et al. 2022, 2023; Barclay et al. 2023), and LHS 475b (Lustig-Yaeger et al. 2023) to strongly suggest that highly-irradiated terrestrial exoplanets orbiting M dwarfs are not capable of retaining low-mean-molecular-weight atmospheres, if they are able to accrete them in the first place. It is possible, however, that LTT 1445Ab possesses a high-mean-molecular-weight or cloudy/hazy atmosphere, which would fall below our detection limits, or no atmosphere at all. To determine whether or not a compact, high-mean-molecular-weight atmosphere is present around this world, James Webb Space Telescope Cycle 1 GO Program 2708 (PI Z. Berta-Thompson) will observe secondary eclipses of this world at mid-infrared wavelengths and search for signs of energy advection that would imply the presence of an atmosphere.

This work is made possible by the dedicated astronomers, telescope operators, instrument specialists, engineers, administrators, and support staff at Las Campanas Observatory. We are grateful to Yuri Beletsky for executing the observations used in this work. We thank Dave Osip and Andreas Seifahrt for extensive conversations about the capability of Magellan II and LDSS3C to collect these data. We thank Jennifer Winters for helpful communications regarding stellar and planetary parameters of LTT 1445A and LTT 1445Ab, Amber Medina for fruitful discussions about Hα variability in M dwarfs, and Jonathan Irwin for contributions to the original observing proposal. We thank Matej Malik for sharing the custom opacity tables used in this work. We thank the Exoplanet Group at DTU Space for insightful conversations during the preparation of this manuscript. We thank the anonymous referee for their comments.

This research has made use of the Exoplanet Follow-up Observation Program website and the NASA Exoplanet Archive, which are operated by the California Institute of Technology, under contract with the National Aeronautics and Space Administration under the Exoplanet Exploration Program. The data analysis described in this work was performed with the help of the high performance cluster at the DTU Computing Center (DTU Computing Center 2021). This material is based upon work supported by the National Aeronautics and Space Administration under grant No. 80NSSC18K0476 issued through the XRP Program. This project is partly funded by Villum Fonden.

Facility: Magellan:Clay (LDSS3C multiobject spectrograph).

Software: `astropy` (Robitaille et al. 2013; Price-Whelan et al. 2018), `batman` (Kreidberg 2015), `decorrasaurus` (Diamond-Lowe et al. 2020a), `dynesty` (Speagle 2020), `Exo-Transmit` (Kempton et al. 2017), `FastChem` (Stock et al. 2018), `george` (Ambikasaran et al. 2015), `HELIOS-K` (Grimm et al. 2021), `LDTk` (Parviainen & Aigrain 2015), `mosasaurus` (http://www.github.com/zkbt/mosasaurus).

ORCID iDs

Hannah Diamond-Lowe https://orcid.org/0000-0001-8274-6639
João M. Mendonça https://orcid.org/0000-0002-6907-4476
David Charbonneau https://orcid.org/0000-0002-9003-484X
Lars A. Buchhave https://orcid.org/0000-0003-1605-5666

References

Ambikasaran, S., Foreman-Mackey, D., Greengard, L., Hogg, D. W., & O'Neil, M. 2015, ITPAM, 38, 252
Azzam, A. A. A., Tennyson, J., Yurchenko, S. N., & Naumenko, O. V. 2016, MNRAS, 460, 4063
Barber, R. J., Tennyson, J., Harris, G. J., & Tolchenov, R. N. 2006, MNRAS, 368, 1087
Barclay, T., Sheppard, K. B., Latouf, N., et al. 2023, arXiv:2301.10866
Borucki, W. J., Koch, D. G., Dunham, E. W., & Jenkins, J. M. 1997, in ASP Conf. Ser. 119, Planets Beyond the Solar System and the Next Generation of Space Missions, ed. D. Soderblom (San Francisco, CA: ASP), 153
Brown, A., Froning, C. S., Youngblood, A., et al. 2022, AJ, 164, 206
Burrows, A., Marley, M. S., & Sharp, C. M. 2000, ApJ, 531, 438
Burrows, A., & Volobuyev, M. 2003, ApJ, 583, 985
Damiano, M., Hu, R., Barclay, T., et al. 2022, AJ, 164, 225
de Wit, J., Wakeford, H. R., Gillon, M., et al. 2016, Natur, 537, 69
de Wit, J., Wakeford, H. R., Lewis, N. K., et al. 2018, NatAs, 2, 214
Diamond-Lowe, H., Berta-Thompson, Z., Charbonneau, D., Dittmann, J., & Kempton, E. M. R. 2020a, AJ, 160, 27
Diamond-Lowe, H., Berta-Thompson, Z., Charbonneau, D., & Kempton, E. M. R. 2018, AJ, 156, 42
Diamond-Lowe, H., Charbonneau, D., Malik, M., Kempton, E. M. R., & Beletsky, Y. 2020b, AJ, 160, 188
Dressing, C. D., & Charbonneau, D. 2013, ApJ, 767, 95
Dressing, C. D., & Charbonneau, D. 2015, ApJ, 807, 45
Dressing, C. D., Charbonneau, D., Dumusque, X., et al. 2015, ApJ, 800, 135
DTU Computing Center 2021, DTU Computing Center Resources, Technical University of Denmark, doi:10.48714/DTU.HPC.0001
Espinoza, N., & Jordán, A. 2016, MNRAS, 457, 3573
Fressin, F., Torres, G., Charbonneau, D., et al. 2013, ApJ, 766, 81
Fulton, B. J., Petigura, E. A., Howard, A. W., et al. 2017, AJ, 154, 109
Gillon, M., Jehin, E., Fumel, A., Magain, P., & Queloz, D. 2013, EPJWC, 47, 03001
Gordon, I. E., Rothman, L. S., Hill, C., et al. 2017, JQSRT, 203, 3
Grimm, S. L., Malik, M., Kitzmann, D., et al. 2021, ApJS, 253, 30
Harris, G. J., Tennyson, J., Kaminsky, B. M., Pavlenko, Y. V., & Jones, H. R. A. 2006, MNRAS, 367, 400
Henry, T. J., Jao, W.-C., Subasavage, J. P., et al. 2006, AJ, 132, 2360
Irwin, J. M., Berta-Thompson, Z. K., Charbonneau, D., et al. 2015, in 18th Cambridge Workshop on Cool Stars, Stellar Systems, and the Sun, ed. G. van Belle et al. (Berlin: Springer), 767
Kempton, E. M.-R., Lupu, R., Owusu-Asare, A., Slough, P., & Cale, B. 2017, PASP, 129, 044402
Koll, D. D. B., Malik, M., Mansfield, M., et al. 2019, ApJ, 886, 140
Kreidberg, L. 2015, PASP, 127, 1161
Kreidberg, L., Koll, D. D. B., Morley, C., et al. 2019, Natur, 573, 87
Kurucz, R. L. 2011, CaJPh, 89, 417
Lavie, B., Bouchy, F., Lovis, C., et al. 2022, arXiv:2210.09713
Lee, H.-W., & Kim, H. I. 2004, MNRAS, 347, 802
Lee, K.-G., Berger, E., & Knapp, G. R. 2010, ApJ, 708, 1482
Li, G., Gordon, I. E., Rothman, L. S., et al. 2015, ApJS, 216, 15
Libby-Roberts, J. E., Berta-Thompson, Z. K., Diamond-Lowe, H., et al. 2022, AJ, 164, 59
Lopez, E. D., & Fortney, J. J. 2013, ApJ, 776, 2

Luque, R., & Pallé, E. 2022, Sci, 377, 1211
Lustig-Yaeger, J., Fu, G., May, E. M., et al. 2023, arXiv:2301.04191
Malik, M., Grosheintz, L., Mendonça, J. M., et al. 2017, AJ, 153, 56
Malik, M., Kempton, E. M. R., Koll, D. D. B., et al. 2019a, ApJ, 886, 142
Malik, M., Kitzmann, D., Mendonça, J. M., et al. 2019b, AJ, 157, 170
Medina, A. A., Charbonneau, D., Winters, J. G., Irwin, J., & Mink, J. 2022, ApJ, 928, 185
Medina, A. A., Winters, J. G., Irwin, J. M., & Charbonneau, D. 2020, ApJ, 905, 107
Mendonça, J. M., & Buchhave, L. A. 2020, MNRAS, 496, 3512
Mendonça, J. M., Malik, M., Demory, B.-O., & Heng, K. 2018, AJ, 155, 150
Mendonça, J. M., Read, P. L., Wilson, C. F., & Lee, C. 2015, P&SS, 105, 80
Miller-Ricci Kempton, E., Zahnle, K., & Fortney, J. J. 2012, ApJ, 745, 3
Mugnai, L. V., Modirrousta-Galian, D., Edwards, B., et al. 2021, AJ, 161, 284
Newton, E. R., Irwin, J., Charbonneau, D., et al. 2016, ApJ, 821, 93
Newton, E. R., Mondrik, N., Irwin, J., Winters, J. G., & Charbonneau, D. 2018, AJ, 156, 217
Nutzman, P., & Charbonneau, D. 2008, PASP, 120, 317
Owen, J. E., Shaikhislamov, I. F., Lammer, H., Fossati, L., & Khodachenko, M. L. 2020, SSRv, 216, 129
Owen, J. E., & Wu, Y. 2013, ApJ, 775, 105
Parviainen, H., & Aigrain, S. 2015, MNRAS, 453, 3821
Price-Whelan, A. M., Sipőcz, B. M., Günther, H. M., et al. 2018, AJ, 156, 123
Rackham, B., Espinoza, N., Apai, D., et al. 2017, ApJ, 834, 151
Richard, C., Gordon, I. E., Rothman, L. S., et al. 2012, JQSRT, 113, 1276
Ricker, G. R., Winn, J. N., Vanderspek, R., et al. 2015, JATIS, 1, 014003
Robertson, P., Bender, C., Mahadevan, S., Roy, A., & Ramsey, L. W. 2016, ApJ, 832, 112
Robitaille, T. P., Tollerud, E. J., Greenfield, P., et al. 2013, A&A, 558, A33
Rogers, L. A. 2015, ApJ, 801, 41
Rothman, L. S., Gordon, I. E., Barber, R. J., et al. 2010, JQSRT, 111, 2139
Seager, S., & Deming, D. 2009, ApJ, 703, 1884
Showman, A. P., Fortney, J. J., Lewis, N. K., & Shabram, M. 2013, ApJ, 762, 24
Sneep, M., & Ubachs, W. 2005, JQSRT, 92, 293
Sousa-Silva, C., Al-Refaie, A. F., Tennyson, J., & Yurchenko, S. N. 2015, MNRAS, 446, 2337
Speagle, J. S. 2020, MNRAS, 493, 3132
Stevenson, K. B., Bean, J. L., Seifahrt, A., et al. 2016, ApJ, 817, 141
Stock, J. W., Kitzmann, D., Patzer, A. B. C., & Sedlmayr, E. 2018, MNRAS, 479, 865
Van Eylen, V., Agentoft, C., Lundkvist, M. S., et al. 2018, MNRAS, 479, 4786
Winters, J. G., Cloutier, R., Medina, A. A., et al. 2022, AJ, 163, 168
Winters, J. G., Medina, A. A., Irwin, J. M., et al. 2019, AJ, 158, 152
Wordsworth, R. 2015, ApJ, 806, 180
Yurchenko, S. N., Barber, R. J., & Tennyson, J. 2011, MNRAS, 413, 1828
Yurchenko, S. N., & Tennyson, J. 2014, MNRAS, 440, 1649
Zhou, L., Ma, B., Wang, Y., & Zhu, Y. 2022, AJ, 164, 203
Zhou, L., Ma, B., Wang, Y.-H., & Zhu, Y.-N. 2023, RAA, 23, 025011